ASME Journal of Autonomous Vehicles and Systems
Online journal at:
https://asmedigitalcollection.asme.org/autonomousvehicles

Smart Chemical Sensing Payload for Emergency Response Uncrewed Autonomous Systems

Jacob M. Anderson
Dynamics and Autonomous Robotics Lab,
Department of Mechanical Engineering and
Robotics Center,
University of Utah,
Salt Lake City, UT 84112
e-mail: Jacob.M.Anderson@utah.edu

Kam K. Leang[1]
Fellow ASME
Dynamics and Autonomous Robotics Lab,
Department of Mechanical Engineering and
Robotics Center,
University of Utah,
Salt Lake City, UT 84112
e-mail: kam.k.leang@utah.edu

A novel smart-sensor payload for uncrewed autonomous systems and emergency responders that automatically detects, estimates, and locates chemical sources is presented. The smart-sensing device fuses Bayesian inference machine learning with information-theoretic motion planning for fast source estimation and localization. More specifically, chemical concentration is measured by a newly developed microelectromechanical-system (MEMS)-based sensor, the location and size of a chemical leak are estimated by a Bayesian inference machine learning process, and information-theoretic motion planning is used to optimally guide the user or an autonomous mobile robot during the search process to improve the speed and accuracy of localizing and quantifying a leaking gas source. Experiments are performed that compare the device's performance under two different motion planning methods: (1) moving the device as instructed by the information-based, guided motion planner and (2) randomly moving the device for search (baseline approach). By following the device's visual cues on where to take measurements (guided motion method), on average, the smart chemical sensor locates a source over 170% faster than moving the sensor randomly (baseline unguided motion method). Additionally, the leak localization error is less than 6.4% (0.325 m). Finally, live methane gas release experiments are performed to further demonstrate the real-world application of the smart handheld chemical sensing device. [DOI: 10.1115/1.4069984]

Keywords: chemical sensing, Bayesian inference, information theory

1 Introduction

Smart and autonomous environmental monitoring systems that leverage advances in sensors and algorithms (machine learning and artificial intelligence methods) can be deployed to collect and analyze environmental data in real-time to support decision-making and mitigate impact when accidents occur [1,2]. Currently, many deployed portable chemical leak detection devices are limited to measuring chemical concentration [3] and do not provide the user any information on source-term estimates and/or the leak location. Instead, the user manually processes the concentration measurements offline to find a leak, which is a slow, inefficient, and imprecise process.

This article describes the development and validation of a new smart, portable, and low-cost chemical gas leak detection device that can be used by an emergency responder or easily integrated with an uncrewed autonomous system (ground or air) to automatically detect, estimate, and locate the source of dangerous chemical leaks (see Fig. 1). The device uses the advanced microelectromechanical-system (MEMS)-based Molecular Property Spectrometer™ (MPS™) sensor to measure local chemical concentration. The measured chemical concentration value, along with the state (i.e., location) of the device, is processed by a machine learning Bayesian inference algorithm to estimate the source terms and locate the leak. The Bayesian estimator is nonparametric, handles measurement uncertainty, and can be readily adapted to allow for the identification of multiple leak sources within a single search space. The estimation process then outputs posterior information that an information-theoretic motion planner uses to create cues to guide the search by a user or a robot. This process improves both the measurement quality and the speed and accuracy of the estimation process. Specifically, the device instructs the user to move toward a region with the highest information gain to minimize measurement uncertainty. No handheld portable gas detection system with similar capabilities has been developed or reported, to the best of the knowledge of the authors. Therefore, the main contribution of this work is the development of such a portable device that fuses machine learning with information-theoretic motion planning for fast source-term estimation and localization. Furthermore, a prototype device is created, and extensive hardware-in-the-loop (HIL) experiments and live gas release demonstrations are performed to test the hypothesis that, by using the new smart chemical gas finder and following its suggestion on how to move, on average: (a) the source localization time is faster and (b) the source localization error is lower than randomly moving the device during search.

On average, a major gas leak event occurs every 40 h in the United States [4]. Unfortunately, the rate of major incidents has not reduced significantly between 2010 and 2021 despite efforts to do so [4]. Chemical leaks and spills incur financial costs through loss of resources and the need for repairs, endanger the environment, and cause potential injury or loss of life within

[1]Corresponding author.

Manuscript received August 4, 2025; final manuscript received September 22, 2025; published online October 21, 2025. Assoc. Editor: Beshah Ayalew.

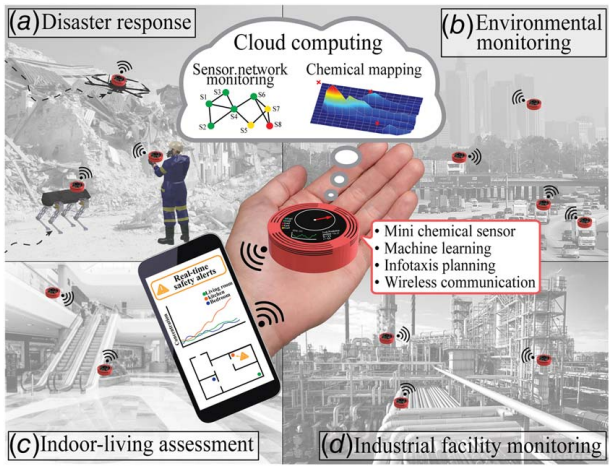

Fig. 1 The smart handheld chemical gas source finding device used to assist in the estimation and localization of chemical gas leaks in (*a*) disaster response, (*b*) air quality monitoring in urban and suburban environments, (c) indoor chemical monitoring, and (*d*) industrial facility monitoring. The device can be integrated with uncrewed aerial and/or ground vehicles or handheld by emergency responders to optimally guide them to find leaks. A network of such devices can be used to create a static or mobile sensor network to expand coverage and enhance performance.

affected communities. To mitigate the effects of chemical leaks, it is important to locate the leak source as quickly and accurately as possible. However, the estimation and localization process is challenging due to chemical plume complexity, measurement uncertainty, health and safety concerns, and environmental conditions [5].

One method to detect and locate the source of a leak is to use a large fixed array of sensors [6,7]. Sensor arrays can effectively localize a source, but they are costly and more practical if the leak source is constrained within a known area, such as a chemical production facility. In the case of natural disasters that occur without warning, fixed sensor arrays are not practical and cannot be readily deployed. On the other hand, mobile robotic systems such as ground and aerial vehicles equipped with sensors and algorithms for source-term estimation and localization are more practical for rapid response in these types of situations [8–12]. Such systems have been developed for radiation detection [13] and search and rescue [14], such as avalanche victim localization [15]. While unmanned autonomous systems (UAS) equipped with sensors can more easily traverse complex terrain and avoid the need to expose human responders to hazards [16], these specialized UAS systems are costly and cannot be used as a handheld unit by emergency responders or easily adapted to other UAS platforms, thus limiting broad application and use.

A low-cost and portable standalone unit with the features of the proposed device has not been described in the literature. Instead, state-of-the-art commercial off-the-shelf portable gas detection devices used by emergency responders only measure and quantitatively report chemical concentration. These devices utilize, for example, electrochemical sensors, flame ionization detectors, metal oxide (MOX) sensors, photo-ionization detectors, gas chromatography-mass spectrometry, etc. [3,17]. Although concentration measurements help identify the presence of a chemical, the task of locating the source requires a large amount of manual effort and time from emergency responders to interpret the information and move the detector to focus on the location of the source. Such a process is seldom automated, and the performance depends on who and how it is used. The proposed device automatically estimates and localizes the source, and the performance can be enhanced through motion planning. By instructing the user on where to move to for measurement, the motion planning algorithm ensures optimal search. Thus, the accuracy of the device is decoupled from the user's experience giving it the advantage that a novice user with minimal training can still operate it effectively.

The remainder of this article is organized as follows. Section 2 describes the features of the device and how it can be used. Section 3 describes the source-term estimation, localization, and motion planning algorithms. Section 4 describes the prototype device. Experiments are described in Sec. 5. Finally, a discussion of results and the conclusions is presented in Sec. 6 and 7, respectively.

2 System Overview

The system architecture is shown in Fig. 2, where the device interacts with a human user (in handheld mode) or can be carried by a mobile robotic system (in smart-sensor payload mode) such as a ground or aerial vehicle, for autonomous chemical source localization. The device consists of a chemical concentration sensor with output measurement $z(t)$. An inverse feedforward compensator, with output $z_f(t)$, accounts for sensor dynamics to improve response time. Next, a Bayesian estimator takes sensor measurement $z_f(t)$, the device's state $\boldsymbol{x}(t)$ (i.e., position), and a prior $[\boldsymbol{\alpha}_0, \boldsymbol{w}_0]$ to generate the posterior distribution $[\boldsymbol{\alpha}(t), \boldsymbol{w}(t)]$, where $\boldsymbol{\alpha}$ is the set that contains predictions of the leak source terms (target estimates) and $\boldsymbol{w}$ is the set of associated importance weights for the estimate set $\boldsymbol{\alpha}$. The posterior distribution is used for motion planning by an information-theoretic algorithm that maximizes information gain for efficient target source-term estimation and localization. The motion planner continuously outputs a desired heading θ_d for the user or the robot to follow and/or process, as needed. The heading points in the direction of the highest information gain between the concentration measurement and source-term estimates. For example, as shown in Fig. 2, the user or the robot can either track the desired heading θ_d (switch S_{fb} closed) or choose to ignore the suggestion from the device and move in an unguided manner (switch S_{ff} closed). It will be shown that following the device's suggested heading ensures that the source-term estimation and localization processes are most efficient.

In addition to outputting the desired heading for the user and/or the robot to follow, the device reports the current predicted source terms $\hat{\boldsymbol{\alpha}}$ of the leak, the current concentration reading z_f in parts per million (ppm), as well as environmental parameters such as temperature, humidity, and air pressure.

When the environment contains hazardous materials or the terrain is difficult for an emergency responder to traverse, the device can be carried by a mobile robot, such as a ground or aerial vehicle, to find leaks without putting a human in harm's way. In this mode, the desired heading θ_d is communicated to the UAS as a reference signal for motion planning and control.

3 Chemical Leak Localization and Estimation

3.1 Measuring Chemical Concentration. The chemical concentration is measured by the MPS™ gas sensor developed by NevadaNano. The MPS™ is a novel MEMS gas sensor that measures the thermodynamic and electrostatic molecular properties of the ambient air/gas mixture that it is exposed to through the use of microhotplates, each coated with semi-selective polymers. The microplates are heated and their thermal properties are used to determine the concentration and identity of the analyte. The sensor is capable of detecting a wide variety of flammable gases, including methane, propane, butane, ethane, ethylene, hexane, hydrogen, isopropanol, pentane, propylene, toluene, and xylene at concentrations from 1% to 100% lower explosive limit (LEL). The sensor boasts good selectivity and maintains concentration measurement accuracy similar to measuring single gases when a mixture of gases is present. Additionally, the sensor enables the determination of the gases present within the environment within six different classes.

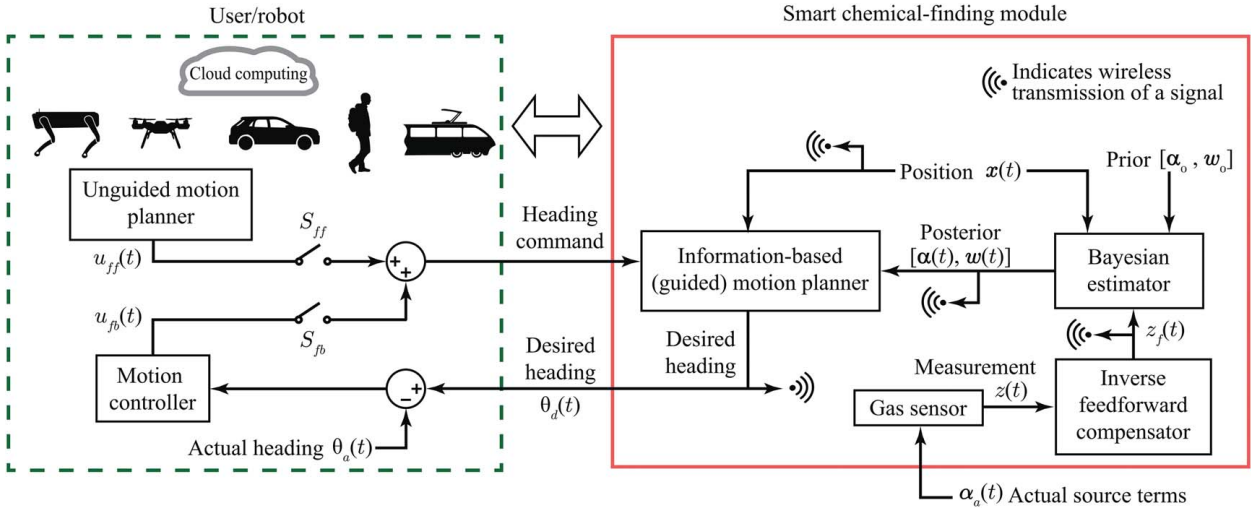

Fig. 2 The basic architecture of the smart chemical gas finding device, consisting of a gas sensor with output $z(t)$ and a leak source-term estimator that generates a posterior $[\alpha(t), w(t)]$, which is fed into an information-based motion planner to calculate a desired heading $\theta_d(t)$. Information from the device is wirelessly transmitted to the interface with cloud computing, human users, robotic platforms, transportation vehicles, etc. The user or the robot can either track the desired heading $\theta_d(t)$ (switch S_{fb} closed) or choose to ignore the suggestion from the device and move in an unguided manner (switch S_{ff} closed).

The MPS^{TM} sensor is also poison-immune, unaffected by sensor drift, lightweight (<4 g), has low operating power consumption (29 mW), and a small form factor (22.9 mm × 26 mm × 5.9 mm). Through collaboration with NevadaNano, the sensor was modified by removing filtering layers to achieve a fast time constant (<1 s) compared to other devices in its class. For example, MOX gas sensors [18,19] and nondispersive infrared gas sensors [20] have response times on the order of 5–8 and 15–30 s, respectively [8]. The MPS^{TM} sensor also offers 1 ppm detection resolution and reports environmental conditions such as temperature, humidity, and pressure.

The specified sensor characteristics, in particular the fast response time, along with a relatively low unit cost (<$100 USD), make the MPS^{TM} sensor excel within mobile sensing applications. This is especially true for applications in handheld systems or as a payload on a robotic platform where the weight and size must be greatly constrained. The MPS^{TM} sensor was chosen for use because other state-of-the-art gas sensors were limited by their slower response times, higher cost, size, or weight.

Methane gas is used throughout the experiments because it is safe to use within the available indoor testing environment at levels well below the LEL, and the MPS^{TM} sensor is capable of measuring and identifying it. The MPS^{TM} was exposed to a methane source, see Fig. 3, and the rise and recover dynamics of the sensor are modeled by a first-order transfer function [8]:

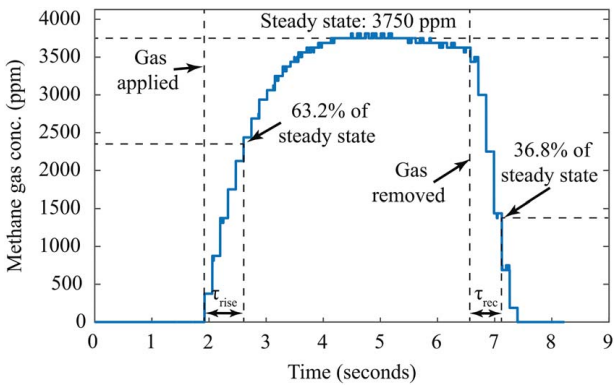

Fig. 3 Response of the MPS^{TM} gas sensor, developed by NevadaNano, during a methane exposure. The measured response shows the rise and recovery time constants.

$$G(s) = \frac{Z_f(s)}{Z(s)} = \frac{b}{\tau s + 1}$$
$$\tau = \begin{cases} \tau_{\text{rise}} & \text{if } \dot{z}(t) > 0 \\ \tau_{\text{rec}} & \text{if } \dot{z}(t) \le 0 \end{cases} \quad (1)$$

where $Z_f(s)$ represents the Laplace transform of the sensor output, $Z(s)$ represents the plume source behavior; b is a scaling factor chosen to be equal to $1/\tau$, and τ_{rise} and τ_{rec} represent the time constants for the rise and recover dynamics measured as 0.606 s and 0.282 s, respectively.

To illustrate the impact of sensor dynamics on chemical concentration mapping using raster-scan movements of the sensor, assume a single source gas release where the leak is modeled by a steady-state Gaussian plume model with concentration expressed as [21]

$$c(x_P, y_P, z_P) = \frac{Q}{4\pi x_P \sqrt{D_y D_z}} \exp\left(-\frac{v}{4x_P}\left(\frac{y_P^2}{D_y} + \frac{z_P^2}{D_z}\right)\right) \quad (2)$$

Here, the concentration c is determined at a point (x_P, y_P, z_P) relative to the plume source location (x_S, y_S, z_S), Q is the source release rate, v represents the wind speed along the x_S direction, and D_y and D_z are the diffusion constants in the y_S and z_S directions, respectively. Additionally, θ_P describes the angle between the defined world x-axis, x_W, and the x_P direction of the plume. These eight source terms fully define the Gaussian plume model and will be represented by the target state vector $\boldsymbol{\alpha} = [x_S, y_S, z_S, Q, v, D_y, D_z, \theta_P]$. The model assumes a steady-state flow from a point source, where advection dominates, and it also neglects diffusion in the x_S direction.

Using this model for the gas source, Fig. 4(*a*) shows an example 2D contour plot of the concentration distribution where the wind direction is parallel to the positive x-axis. The plume source terms in this example are: $\boldsymbol{\alpha} = [0.5\text{ m}, 1.5\text{ m}, 0.2\text{ m}, 0.15\text{ kg/s}, 4.0\text{ m/s}, 4.0 \times 10^{-1}\text{ m}^2/\text{s}, 3.0 \times 10^{-3}\text{ m}^2/\text{s}, 0\text{ deg}]$.

To map the plume, the MPS^{TM} gas sensor is moved along a raster-scan trajectory over the area as illustrated in Fig. 4(*a*). The concentration readings are recorded at constant height as the sensor moves, and the measurements are then plotted with respect to the sensor location to create a chemical concentration map.

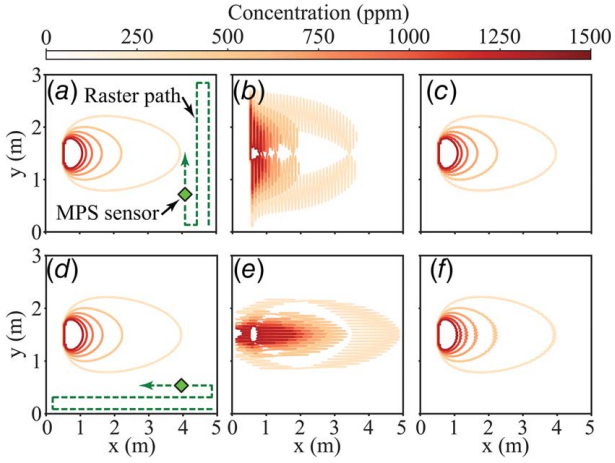

Fig. 4 Simulated chemical concentration maps: (*a*) ground-truth map with a *y*-axis raster trajectory; (*b*) map generated by a simulated MPS™ sensor traveling at a speed of $9.0V_{max}$, showing the effects of sensor dynamics; (*c*) dynamic compensation is applied; (*d*) ground-truth map with a *x*-axis raster trajectory; and (e) and (*f*) are distorted and compensated maps, respectively; *x*-axis raster trajectory at a speed of $5.2V_{max}$

Ignoring sensor dynamics, the contour map in Fig. 4(*a*) represents the simulated chemical concentration distribution.

Considering the sensor dynamics, specifically the rise and recovery time constants of the sensor (see Fig. 3), a conservative theoretical maximum sensor velocity V_{max} can be determined as [8]

$$V_{max} = \frac{d_{max}}{20\pi\tau} \tag{3}$$

where d_{max} is the maximum straight line distance that would be traveled if a raster-scanning pattern were followed over the area being explored. The time constant τ is chosen as the larger time constant between τ_{rise} and τ_{rec}. As the sensor velocity exceeds V_{max}, the measurement quality begins to degrade due to the dynamics of the sensor.

For example, if the sensor is moved at a velocity of $9.0V_{max}$, the resulting chemical concentration map shows distortion within the contours as illustrated in Fig. 4(*b*). Thus, the results misrepresent the true distribution shown in Fig. 4(*a*). Sensor dynamics can significantly affect mapping and source-term estimation performance and thus need to be accounted for.

An inverse feedforward compensator is applied to account for sensor dynamics to further improve performance and allow the sensor to be moved faster than V_{max} without significantly degrading the measurement quality. The feedforward compensator is

$$G_{lp}^{-1}(s) = \frac{(\tau s + 1)\gamma}{b(s+\gamma)} \tag{4}$$

where γ represents the low-pass filter time constant chosen to be equal to ten times the sensor time constant ($\gamma = 10\tau$). It is also noted that the low-pass filter time constant is inversely proportional to the filter's cutoff frequency. Therefore, as γ is increased, more high-frequency content within the measured signal will be attenuated. The discrete-time form used for implementation is given by

$$z_f[k] = \frac{z[k]\left(\frac{\gamma}{\tau} + \frac{\gamma}{\Delta t}\right) - z[k-1]\frac{\gamma}{\Delta t} + z_f[k-1]\frac{b}{\tau\Delta t}}{\frac{\gamma b}{\tau} + \frac{h}{\tau\Delta t}} \tag{5}$$

where k denotes the current time instant, $k-1$ denotes the previous time instant, Δt represents the effective time-step, and $z_f[k]$ represents the compensated sensor output.

The results in Fig. 4 show the effects in simulation of using the MPS™ for chemical-concentration mapping. In Figs. 4(*b*) and 4(*c*), the sensor travels in a raster trajectory along the *y*-axis at a speed of $9.0V_{max}$. Figures 4(*e*) and 4(*f*) show the simulated maps for a raster trajectory along the *x*-axis at speed $5.2V_{max}$. In each case, sensor dynamics cause the resulting concentration contours to smear. However, by applying dynamic compensation, the original Gaussian plume contour map is recovered at speeds larger than the theoretical V_{max} as shown in Figs. 4(*c*) and 4(*f*). In the following sections, the output $z_f(t)$ of the feedforward compensator is used by the source-term estimation process.

3.2 Source-Term Estimation Process Via Machine Learning. The chemical concentration measurement $z_f(t)$, the prior source-term knowledge, and the device's state $\boldsymbol{x}(t)$ are processed by a Bayesian estimator to generate a posterior density (Fig. 2) to predict the unknown chemical leak source terms $\boldsymbol{\alpha} = [x_S, y_S, z_S, Q, v, D_y, D_z, \theta_P] \in \boldsymbol{A} \in \mathbb{R}^8$ [22]. The posterior density is found by Bayes' rule:

$$p(\boldsymbol{\alpha}[k]|z_f[k_0:k]) = \frac{p(z_f[k]|\boldsymbol{\alpha}[k])p(\boldsymbol{\alpha}[k]|z_f[k_0:k-1])}{p(z_f[k]|z_f[k_0:k-1])} \tag{6}$$

where $p(\boldsymbol{\alpha}[k]|z_f[k_0:k-1])$ is the prior, $p(z_f[k]|\boldsymbol{\alpha}[k])$ is the likelihood, and $p(z_f[k]|z_f[k_0:k-1])$ is the marginal likelihood.

First, a prior distribution $p(\boldsymbol{\alpha}[k]|z_f[k_0:k-1])$ is chosen to initialize the Bayesian estimator. A uniform distribution $U(\boldsymbol{A})$ over the target source-term space $\boldsymbol{A}$ is chosen, but any available knowledge about the source terms can be used to initialize the estimator.

Next, the likelihood $p(z_f[k]|\boldsymbol{\alpha}[k])$ is determined through a likelihood model. In this case, the chosen likelihood model is the Gaussian plume model shown in Eq. (2), which equates the time-averaged gas concentration c of a plume with source terms $\boldsymbol{\alpha}$ at a specified position. This model has been used extensively to characterize many physical plumes [23,24], and more recently as a likelihood model for Bayesian estimation of a chemical leak [10,25]. This model is used to determine an expected concentration measurement $g_i[k]$ from the current location of the device with respect to each estimate (particle) $\boldsymbol{\alpha}_i$. The larger the difference between the expected value $g_i[k]$ and the current measurement $z_f[k]$, the lower the probability of the particle $\boldsymbol{\alpha}_i[k]$, i.e.,

$$p(z_f[k]|\boldsymbol{\alpha}_i[k]) = N(z_f[k];\, g_i[k],\, r(\sigma_{(x_S,y_S,z_S)}[k])) \tag{7}$$

where $N(\cdot)$ is a normal distribution over a likelihood deviation $r(\cdot)$ dependant on the posterior [10]

$$r(\sigma_{(x_S,y_S,z_S)}[k]) = q\frac{\|\sigma_{(x_S,y_S,z_S)}[k]\|_2}{\max_{\forall k}\left(\|\sigma_{(x_S,y_S,z_S)}[k]\|_2\right)} \tag{8}$$

In (8), $\sigma_{(x_S,y_S,z_S)}[k]$ denotes the vector of the standard deviations of the estimated plume locations (x_S, y_S, z_S) at time-step k and $q \in \mathbb{R}^+$, with $\mathbb{R}^+$ representing the set of positive real numbers, is the initial likelihood standard deviation.

The Bayesian estimator is implemented using a Monte Carlo approach in the form of a particle filter (PF) to iteratively update the posterior prediction as new measurements are taken. The PF uses a nonparametric approximation of the posterior distribution as a sum of weighted source-term particles. The posterior and prior approximations are denoted by $[\boldsymbol{\alpha}[k], \boldsymbol{w}[k]]$ and $[\boldsymbol{\alpha}_0, \boldsymbol{w}_0]$, respectively. The PF is expressed as [26]

$$p(\boldsymbol{\alpha}[k]|z_f[k_0:k]) \approx \sum_{i=1}^{\eta} w_i[k]\delta(\boldsymbol{\alpha}[k] - \boldsymbol{\alpha}_i[k]) \tag{9}$$

where η represents the total number of particles, $\delta(\cdot)$ is the Dirac delta function, and $\boldsymbol{\alpha}_i$ denotes the ith particle with associated importance weight w_i such that $\sum_{i=1}^{\eta} w_i = 1$. If at each time-step the new particle distribution is sampled from the prior distribution, the importance weight is proportional to (7) and can be defined as [26]

$$w_i[k] \propto w_i[k-1]p(z_f[k]|\boldsymbol{\alpha}_i[k]) \tag{10}$$

During each iteration of the Monte Carlo process, the best guess of the true plume parameters is determined by the minimum mean-squared estimate (MMSE) approximation:

$$\hat{\boldsymbol{\alpha}}[k] \approx \sum_{i=1}^{\eta} w_i[k]\boldsymbol{\alpha}_i[k] \tag{11}$$

The posterior distribution $[\boldsymbol{\alpha}[k], w[k]]$ is then refocused onto particles with large importance weights, and the importance weight of each particle is reset to $w = 1/\eta$ to prevent degeneracy of the distribution [26]. The refocusing process is achieved through a systematic resampling method selected because of the linear complexity $O(n)$ of the method and its low variance [22]. Additionally, when the resampling occurs, Gaussian noise is applied for each particle, where the standard deviations of the noise for each source term are denoted by $(\sigma_x, \sigma_y, \sigma_z, \sigma_\theta, \sigma_Q, \sigma_v, \sigma_{D_y}, \sigma_{D_z})$. This step helps prevent sample impoverishment [26]. The estimated posterior $[\boldsymbol{\alpha}[k], \boldsymbol{w}[k]]$ is refined at each time-step and by the information-theoretic motion planner as described in the following section.

An advantage of this approach to leak source-term estimation is that the posterior distribution is multimodal by nature and can easily be extended to situations with multiple leaking sources. When concentration readings are taken within areas of overlapping leak sources, the estimator can identify multiple likely leak sources contributing to the readings and explore each of them independently through the information-theoretic motion planner (Sec. 3.3). Additionally, after a leaking source has been identified, the area can continue to be explored, and the anticipated concentrations due to previously identified leaks can be accounted for, allowing for the identification of any additional unmodeled sources within the search space.

3.3 Motion Planning. Information-based motion planning has been used to assist in reducing source estimate uncertainty during searches [11,27,28]. The information-based motion planner uses the posterior $[\boldsymbol{\alpha}[k], \boldsymbol{w}[k]]$ and the device's state $\boldsymbol{x}(t)$ to generate a desired heading θ_d for the user of the device to follow. To do this, the local mutual information surface between measurements z_f and source-term estimates $\boldsymbol{\alpha}$ over the search area at time-step k is created. Next, relative to the current location of the device, the point of the highest amount of mutual information is determined, which is then used to compute the heading direction θ_d for the device. If the device is moved in this direction, then measurement uncertainty is minimized and the Bayesian estimation process is most effective.

Specifically, mutual information is computed by

$$\begin{aligned} I(z_f[k]; \boldsymbol{\alpha}[k] | \boldsymbol{z}_f[k_0 : k-1]) &= I(z_f[k]; \boldsymbol{\alpha}[k]) \\ &= H(z_f[k]) - H(z_f[k]|\boldsymbol{\alpha}[k]) \end{aligned} \tag{12}$$

where $H(z_f[k])$ denotes the Shannon entropy of the measurement and $H(z_f[k]|\boldsymbol{\alpha}[k])$ denotes the Shannon entropy of the measurement conditioned on the source-term estimates [29]. The leak source is assumed to be stationary and unaffected by the location of the device. Using probability distributions approximated by the particle filter posterior, the entropy terms can be expressed as [30,31]

$$\begin{aligned} H(z_f[k]) \approx -\int_{z_f \in \boldsymbol{Z}} \left(\sum_{i=1}^{\eta} w_i[k] p(z_f[k]|\boldsymbol{\alpha}_i[k]) \right) \\ \times \log \left(\sum_{i=1}^{\eta} w_i[k] p(z_f[k]|\boldsymbol{\alpha}_i[k]) \right) \mathrm{d}z_f \end{aligned} \tag{13}$$

$$\begin{aligned} H(z_f[k]|\boldsymbol{\alpha}[k]) \approx -\int_{z_f \in \boldsymbol{Z}} \sum_{i=1}^{\eta} (w_i[k] p(z_f[k]|\boldsymbol{\alpha}_i[k]) \\ \times \log \left(p(z_f[k]|\boldsymbol{\alpha}_i[k]) \right)) \mathrm{d}z_f \end{aligned} \tag{14}$$

where $\boldsymbol{Z} = [\min(z_f), \max(z_f)]$ is the measurement range.

Examples of mutual information surfaces for source term $\boldsymbol{\alpha}$ with $n = 3$ and $n = 3500$ particles are shown in Fig. 5. These surfaces indicate regions of high information (darker shaded areas), and thus the device should be moved to (and take measurements at) these locations to minimize uncertainty and make the Bayesian estimation process more efficient.

Calculating the mutual information at each time-step can be computationally intense. To improve real-time computation performance, first, the integrals in (13) and (14) are solved through Gauss-Legendre quadrature approximation techniques. Second, the local mutual information surface is calculated for a set planar distance r_I from the device's current position and the location of highest information within this space, $\boldsymbol{x}_I = [x_{I,x}, x_{I,y}]$. Finally, the desired heading θ_d is given by

$$\theta_d = \arctan\left(\frac{x_y - x_{I,y}}{x_x - x_{I,x}}\right) \tag{15}$$

and reported to the user or the robot for motion planning. It is noted that the calculation of the mutual information is the dominant process at each update step. Searching over large spaces, the number of particles used can be easily scaled to provide additional estimates over the search space, but the extent to which the range of the local information surface, r_I, can be extended may be limited. However, this could be improved through particle subsampling over a larger local region to determine the information surface used by the motion planner or by offloading the heavy mutual information computation to a wirelessly connected ground station computer.

4 Prototype Device Design

A prototype device (see Figs. 6 and 7 for the device mounted on a mobile ground robot) was created for testing and evaluation. The device is 152 mm (~ 6 in.) in diameter and 54 mm (~ 2 − 1/8 in.) tall. The housing and internal structures were 3D printed from polylactic acid (PLA) plastic. The material cost to develop the device is less than $280 USD. Figure 6(*c*) shows the main components and the connections between the supporting hardware and the computing system. Specifically, the computational hardware consists of an ODROID-XU4 single-board computer (SBC) with an octa-core CPU (2.0 GHz max core speed), 2 GB RAM, and USB 3.0 ports. All algorithms were implemented under the robot operating system (ROS) and ROS nodes were created to interface the SBC with an MPS™ sensor for measuring chemical concentration. The MPS™ sensor is positioned so that the air intake mesh is flush with the top surface of the device to ensure good exposure of the sensing chamber. An LCD display shows the desired heading θ_d from the motion planning algorithm in the form of a compass needle. The display also displays chemical concentration readings (in units of ppm) and the estimates of the current source terms in $\hat{\boldsymbol{\alpha}}$. The SBC has on-board Wi-Fi for short-range wireless

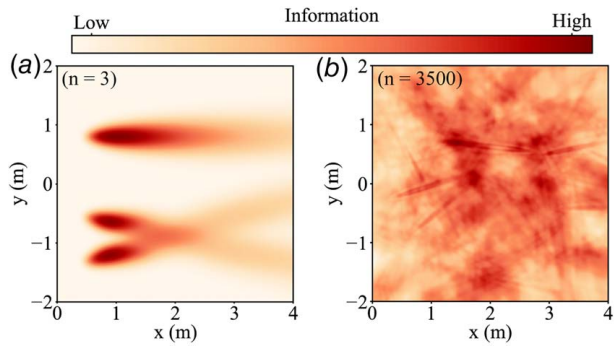

Fig. 5 Mutual information maps for (*a*) $n = 3$ particles and (*b*) $n = 3500$ particles with randomized source terms

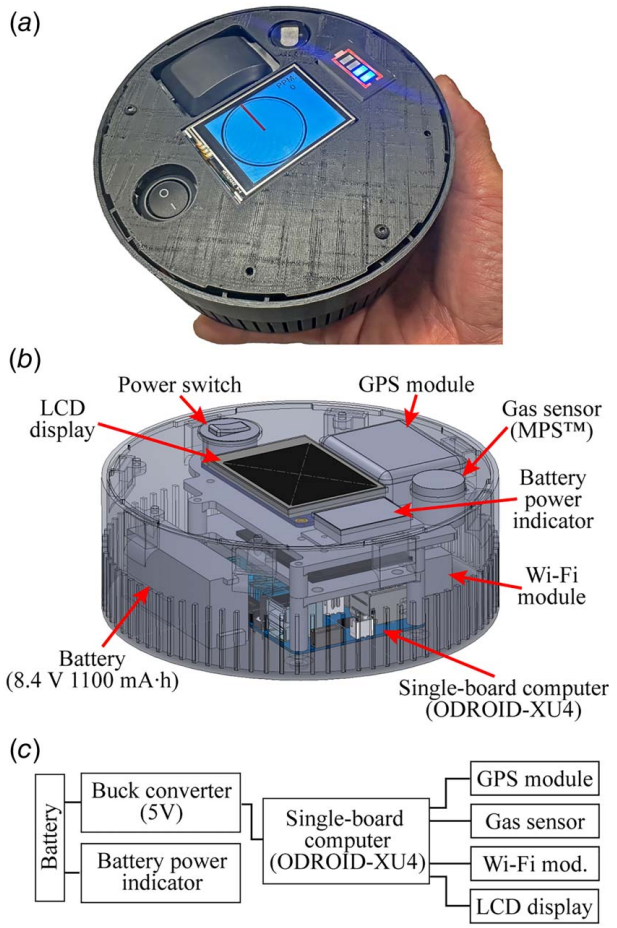

Fig. 6 (*a*) The prototype device operating in the handheld mode, (*b*) computer-aided design (CAD) model of the device showing internal key components, and (c) major components and their connections

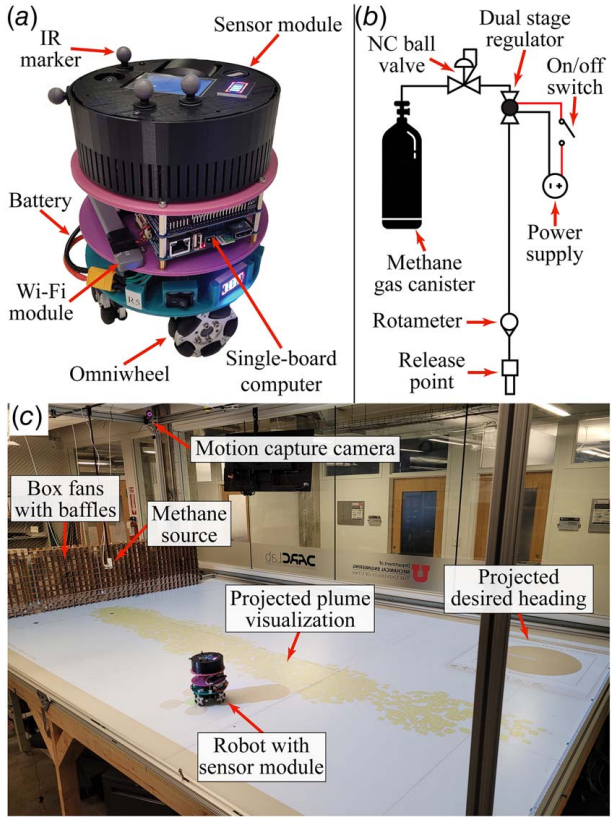

Fig. 7 The experimental setup: (*a*) mobile ground robot carrying the smart-sensor payload, (*b*) the methane release system for live chemical leak experiments, and (c) the testing environment with gas leak source

communication with a local command station for remote data logging and visualization. The device is equipped with a global positioning system (GPS) module to provide state (position) information. The entire device is powered by a 2S 1100-mAh battery as shown in Fig. 6(*c*). The total weight of the device is approximately 400 g (0.88 lbs).

5 Experiments and Demonstration

5.1 Experimental Setup. The device is mounted to a custom-built omniwheel robot (Fig. 7(*a*)). This allows consistent control of the speed of the device during each experiment. The robot's motion is controlled by an ODROID-XU4 SBC that runs ROS and interfaces with a Robotis U2D2 for motor control. The robot is equipped with potential-field collision avoidance and is controlled to move freely throughout the search space.

The plume source, using the release system shown in Fig. 7(*b*), is located at $\boldsymbol{x}_T = [0.64, 1.07, 0.40]$ m, relative to the bottom left corner of the test volume, shown in Fig. 7(*c*). The elevated platform measures 4.3 m (14 ft) × 2.7 m (9 ft) × 1.8 m (6 ft). When methane gas is released, box fans with baffles create a relatively uniform flow with a wind speed of approximately 2.0 m/s over the test surface.

A motion capture camera system (10 OptiTrack Flex 13 cameras) tracks the motion of the device mounted on a mobile robot platform. The motion capture system has a sampling frequency of 120 Hz. A light-emitting diode projector projects and visualizes a simulated plume on the surface of the platform during experiments. The desired heading θ_d is also projected onto the test platform surface to inform the operator how to control the movements of the robotic system.

The robot can be controlled to move on the test surface for source-term estimation and localization. The robot ensures that the device is moved at a controlled desired speed and that the height of the sensor above the ground remains constant during the experiments. A conservative $V_{\max}$ is calculated using the maximum distance the device could move if following a raster pattern along the platform width (2.0 m) for $d_{\max}$ and the slower time constant between the rise and recover dynamics of the sensor (0.606 s). The resultant $V_{\max}$ of the device is 0.053 m/s. Because dynamic compensation is applied to the sensor readings, the robot is set to travel at a maximum speed of 0.1 m/s, approximately two times the calculated $V_{\max}$.

5.2 Performance Via Hardware-in-the-Loop Experiment. The developed device aims to streamline the identification of a leaking chemical source and reduce the effort required by the user to accomplish the task. As such, the performance of the device is evaluated by testing whether, through the use of the device, the localization and estimation of a leak source is improved. To this end, HIL experiments are performed to test the hypotheses that if the user follows the device's suggested heading θ_d while searching for the leak, on average: (a) the source localization time will be much faster and (b) the source localization error will be much lower than if the device was moved in an uninformed way (i.e., unguided random motion). In the experiments, a simulated gas plume (GADEN plume model) is used as the source. The GADEN-generated plume realistically and accurately models gas dispersion through filament gas dispersion theory over a time-evolving wind flow vector field [32]. The reason for using a simulated plume in

this experiment is that the source terms can be precisely controlled so that the experiments can more accurately evaluate the performance of the device's algorithms and test the hypothesis. In fact, creating consistent and precisely controlled physical gas leaks for multiple experimental trials is challenging and not within the scope of this work.

For the HIL experiments, two different motion planning methods are compared: (1) guided motion achieved by moving in the direction of the desired heading θ_d as determined by the device and (2) randomly moving the device within the search space simulating the movement if a device is incapable of guiding the user. For the experiments, the following assumptions were made about the source: (1) position remains stationary, (2) parameters $\boldsymbol{\alpha}$ are bounded by $\boldsymbol{A}$, and (3) source height is known. The source-term search space is constrained to $\boldsymbol{A}$ so that only leak sources of sizes appropriate to the relative scale of the experimental space were considered, reducing some computational effort of the particle filter. It is noted that the algorithm could easily be altered to consider much smaller or larger sources. Additionally, because the source height is assumed to be known, the dimensionality of the estimation process is reduced, which improves computational efficiency. However, these parameters could be altered to account for height variability in the leaking source with minimal effort. The parameters of the simulated GADEN plume are shown in Table 1, while the parameters of the Bayesian estimator (particle filter) are shown in Table 2. Finally, although the leak rates used within the experiments are fixed, the algorithm does not assume this fact. The Gaussian plume model estimated by the algorithm represents the best time-averaged fit for the concentrations seen within the environment. Thus, if the leak source parameters were to vary over time, the algorithm would estimate a model with parameters associated with the median concentration ranges seen spatially throughout the search space.

For the HIL experiments, the device samples the concentration of the simulated GADEN plume at each specific location in the environment [32]. The robot starts each trial at $\boldsymbol{x} = [3.6, 0.25]$ m. This location was chosen as it represents one of the more challenging start locations as it will not initially measure any concentration readings and will have to explore the space to do so. Additionally, the position makes it unlikely to randomly happen upon areas of very high concentration which quickly allow for the leak to be identified.

Table 1 GADEN-generated plume simulation parameters

Parameter	Description	Value
Δt_g	Time-step for plume updates	0.1 s
F_s	Filament release rate	350 filaments/s
F_c	Concentration at the center of the filament	90–110 ppm
F_σ	Initial shape of the filament	3 cm
F_γ	Growth ratio	3 cm/s^2
F_q	Additive white noise	0.03 m
T	Temperature	298 K
P	Pressure	1 atm

Table 2 Parameters of the particle filter used during the HIL experiment

Particle filter parameters for simulated GADEN plume
$A = x_s \in [0.3, 3.6]$ m, $y_s \in [0.27, 2.3]$ m, $z_s \in [0.2, 0.2]$ m,
$\theta \in [-10.0 \text{ deg}, 10.0 \text{ deg}]$,
$Q \in [0.7, 1.5]$ kg/s, $v \in [2.0, 4.0]$ m/s, $D_y \in [5.0 * 10^{-3}, 5.0 * 10^{-2}]$ m^2/s,
$D_z \in [5.0 * 10^{-3}, 3.0 * 10^{-2}]$ m^2/s
$\sigma_x = 0.018$ m, $\sigma_y = 0.018$ m, $\sigma_z = 0.0$ m, $\sigma_\theta = 0.0055$ deg, $\sigma_Q = 0.015$ kg/s,
$\sigma_v = 0.01$ m/s, $\sigma_{D_y} = 0.01$ m^2/s, $\sigma_{D_z} = 0.01$ m^2/s
$t_{\max} = 650$ s, $\eta = 3500$, $\boldsymbol{\alpha}_0 = \mathcal{U}(A)$, $q = 650$ ppm

Finally, the position is maintained between experiments to allow for fair comparisons between the time required to localize the leak source, while the effects of spatial position on the performance of the estimation can still be explored by evaluating the trajectories taken during each experimental trial. The HIL experiment consisted of 30 trials for the guided motion method (following desired heading θ_d) and 30 trials for the unguided motion method (random motion).

5.3 Demonstration: Finding a Methane Gas Leak. Following the HIL experiment, the device is used to localize a physical methane gas leak to demonstrate the basic functionality of the device in a near-real-world scenario. Here, the device was also moved by following the device's heading angle θ_d and moving it in a random fashion.

The methane gas source leak rate during the demonstration is 7.88×10^{-5} kg/s (15 standard cubic feet per hour). Three trials were run for the guided motion method and three trials for the unguided motion. The particle filter parameters are shown in Table 3.

5.4 Performance Metrics. The metrics by which the device's performance was quantified are the time to localize the leak and the localization error (error between the estimated leak location and the true leak location). The localization time is defined as the time when the two-norm of the standard deviation of the source location estimate σ_T is below the threshold σ_c, i.e.,

$$\sigma_T = \sqrt{\sigma_{x_s}^2 + \sigma_{y_s}^2} < \sigma_c \tag{16}$$

where $\sigma_c = 0.12$ m. The localization was deemed successful when the device's performance met this threshold within the allotted 650-s ($t_{\max}$) time window.

The localization error e_d, the distance from the predicted plume location $(\hat{\alpha}_{x_s}, \hat{\alpha}_{y_s})$ to the true plume location $(x_{T,x}, x_{T,y})$, is calculated as a percentage of the range of the search area:

$$e_d = \frac{\sqrt{(x_{T,x} - \hat{\alpha}_{x_s})^2 + (x_{T,y} - \hat{\alpha}_{y_s})^2}}{\sqrt{(x_U - x_L)^2 + (y_U - y_L)^2}} \times 100 \tag{17}$$

Here, $[x_L, y_L]$ and $[x_U, y_U]$ represent the lower and upper bounds of the x and y components of the search area, respectively; and $(x_{T,x}, x_{T,y})$ represents the ground truth of the leak location.

6 Discussion

6.1 Localization Time Performance. Using guided motion for the HIL experiment, all 30 trials successfully located the plume. The average localization time is 106 s. For the unguided motion, 26 trials successfully located the plume. The average localization time is 186 s. The results are shown in Fig. 8, and they show that the information-based guided motion method localized the source on average 1.76 times faster compared to the random

Table 3 Parameters of the particle filter parameters used during the live methane gas release demonstration

Particle filter parameters for physical methane leak
$A = x_s \in [0.3, 3.8]$ m, $y_s \in [0.2, 2.4]$ m, $z_s \in [0.2, 0.2]$ m,
$\theta \in [-10.0 \text{ deg}, 10.0 \text{ deg}]$,
$Q \in [0.1, 0.5]$ kg/s, $v \in [1.0, 4.0]$ m/s, $D_y \in [1.0 \times 10^{-2}$,
$1.0 \times 10^{-1}]$ m^2/s,
$D_z \in [1.0 \times 10^{-3}, 1.0 \times 10^{-2}]$ m^2/s
$\sigma_x = 0.005$ m, $\sigma_y = 0.005$ m, $\sigma_z = 0.0$ m, $\sigma_\theta = 0.0055$ deg, $\sigma_Q = 0.015$ kg/s
$\sigma_v = 0.01$ m/s, $\sigma_{D_y} = 0.01$ m^2/s, $\sigma_{D_z} = 0.01$ m^2/s
$t_{\max} = 650$ s, $\eta = 3500$, $\boldsymbol{\alpha}_0 = \mathcal{U}(A)$, $q = 820$ ppm

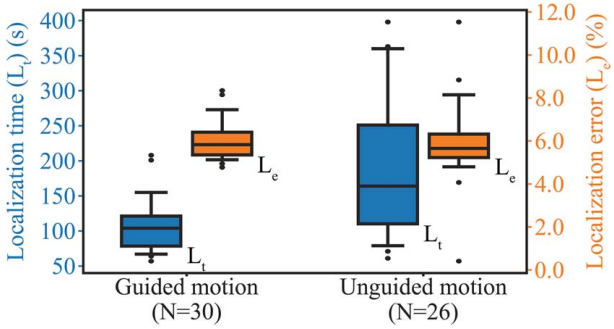

Fig. 8 Localization time (L_t) and localization distance error (L_e) results from the HIL experiment. The left-hand plots show the results from the trials using the guided motion method. The right-hand plots show the results from the trials using the unguided motion method.

Table 4 Localization time and error results from the live methane gas release experiments

	Localization time (s)	Localization error (m)	Localization error (%)
Guided motion trial 1	39.0	0.249	4.9
Guided motion trial 2	90.0	0.466	9.2
Guided motion trial 3	37.0	0.225	4.4
Guided motion average	55.3	0.313	6.2
Unguided motion trial 1	140.0	0.381	7.5
Unguided motion trial 2	197.0	0.513	10.1
Unguided motion trial 3	193.0	0.086	1.7
Unguided motion average	176.7	0.327	6.4

motion method. Application of a Welch's *t*-test using a 99.7% confidence level resulted in $p = 0.00035$, indicating the statistical significance of the difference in average localization times [33]. Thus, the results confirm hypothesis (a) that when following the guided motion, the average source localization time is much faster than the unguided motion method. One observation is that the results from the random motion method had more variability in localization time. It is believed that moving randomly causes the robot to spend more time in areas where the concentration readings are low, which negatively impacts the performance of the Bayesian estimator.

The results for localizing the physical methane gas leak are shown in Table 4. Specifically, one example of the time evolution of the estimated source locations is illustrated in Figs. 9 and 10 for the guided and unguided motion, respectively. Each black dot represents an estimated (x_S, y_S) location of the source, and the orange contours represent a composite Gaussian plume for the MMSE $\hat{\boldsymbol{\alpha}}$ source terms. From Table 4, the average localization time from the guided motion is 55.3 s compared to 176.7 s for the unguided motion. Thus, the guided motion method localized the methane gas leak on average 3.20 times faster than the unguided motion method.

6.2 Localization Error Performance. The median localization distance errors for both the unguided and guided motion methods are 6.0% (0.3 m, see Fig. 8). A Welch's *t*-test using a 99.7% confidence level resulted in $p = 0.92360$, indicating that there is no statistical difference between the two methods' average localization distance error results for the simulated gas leak scenario. Thus, this outcome invalidates the hypothesis (b). Similar to the simulation results, the results of the physical methane leak experiments yielded 6.2% (0.313 m) and 6.4% (0.327 m) average error when the guided motion and unguided motion methods were used, respectively. It can be seen in Fig. 10, where unguided motion was used, that the majority of the measurements taken by the device would have been in areas where concentration readings were low. The results in Fig. 9, where guided motion was used, show that many of the measurements taken were downwind of the leak source where concentration readings are higher. Despite this difference, the plume localization

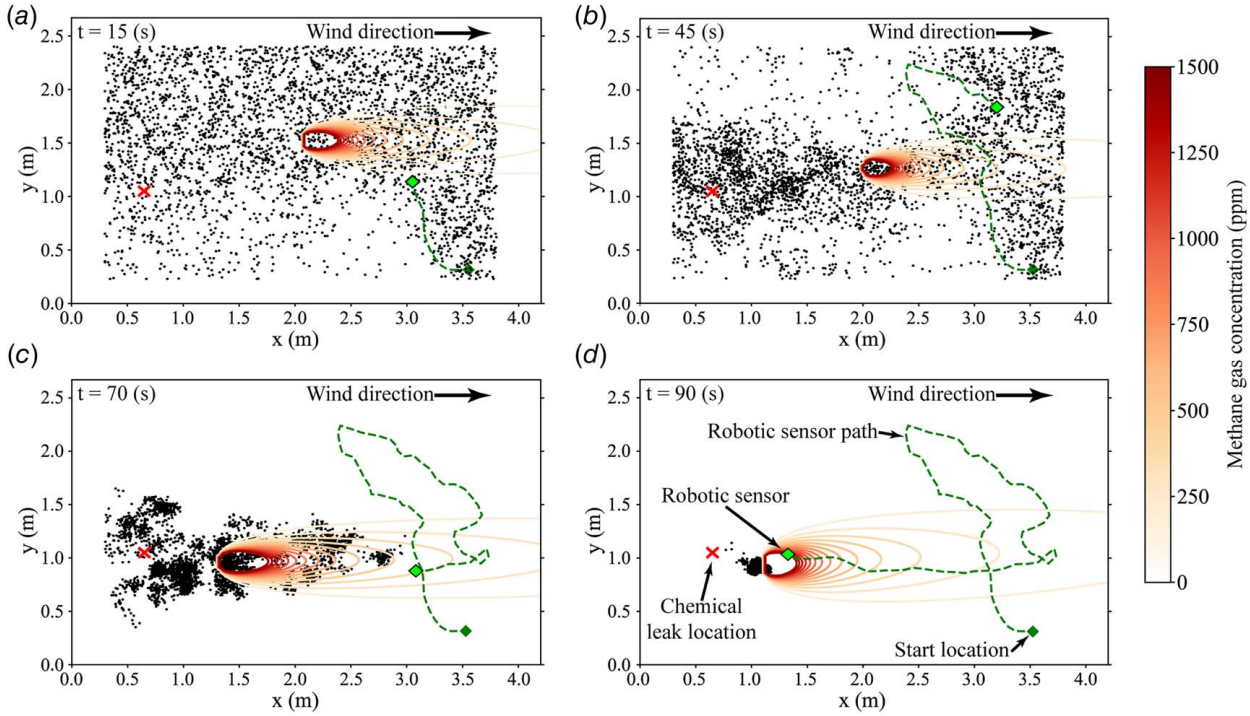

Fig. 9 Experimental results from a live methane leak trial using guided motion showing the distribution of estimated source locations at time intervals: (*a*) 15, (*b*) 45, (*c*) 70, and (*d*) 90 s. The Gaussian plume for the MMSE $\hat{\alpha}$ source terms is represented by the contour curves.

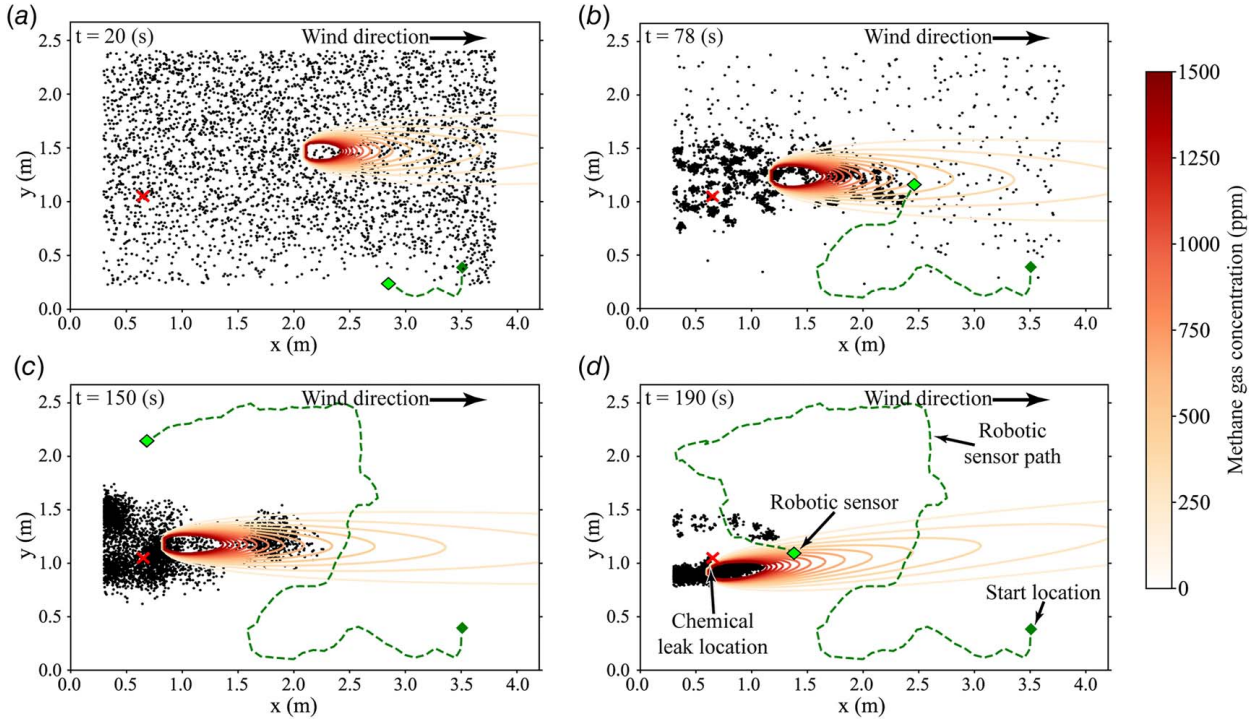

Fig. 10 Experimental results from a live methane leak trial using unguided motion showing the distribution of estimated source locations at time intervals: (*a*) 20, (*b*) 78, (c) 150, and (*d*) 190 s. The Gaussian plume for the MMSE $\hat{\alpha}$ source terms is represented by the contour curves.

errors are comparable, showing that the source-term estimation accuracy was not affected by differences in the time spent in low versus high concentration areas. Thus, the overall accuracy of the source-term estimation process is independent of the type of motion planning used. This result suggests that even novice users can effectively use the device to accurately locate the source. In summary, these results demonstrate the effectiveness of the smart sensor to estimate and localize an unknown leaking chemical source.

6.3 Extension to Unstructured Environments. The demonstrations using live methane gas sources offer good insight into the performance of the device. However, there are still simplifications in place, such as the relatively uniform airflow created within the laboratory setting. In unstructured environments, with dynamic airflow, the estimation process is still expected to perform well. Because the estimation process utilizes a time-averaged concentration model, small fluctuations would not drastically affect the overall performance as the baseline behavior of the leak source will still be identified. In situations where larger changes occur over time, such as the wind direction shifting, or the leak size increasing or diminishing, the leak can be localized and estimated multiple times by continuing the search even after a leak is first identified. This would allow for the time evolution of the leak to be identified through the differences in the estimated leak source terms over the search window. These performance aspects in more complicated environments will be tested in future work.

7 Conclusions

This article focused on the development of a new smart and portable low-cost device that can be handheld by an emergency responder or easily integrated with a UAS to automatically detect, estimate, and localize dangerous chemical leaks. An information-based motion planner guides the user to improve the process of finding the source by over 1.7 times faster compared to randomly moving the device during search. Experiments showed that the overall accuracy of the localization process was not dependent on how the device was moved. In summary, the results demonstrated the basic functionality of the device and its application for localizing a chemical gas leak in near-real-world scenarios.

Acknowledgment

This material is based upon work supported, in part, by the University of Utah and U.S. Air Force STTR Program grant no. F18B-009-0083. Any opinions, findings, and conclusions or recommendations expressed in this document are those of the authors and do not necessarily reflect the views of the sponsors. Authors thank Nevada NanoTech Systems, Inc., for providing a prototype MPS sensor for this work and Chantel Lapins and Sasha McKee for engaging in technical discussions.

Conflict of Interest

There are no conflicts of interest.

Data Availability Statement

The authors attest that all data for this study are included in the article.

References

[1] Rosser, K., Pavey, K., FitzGerald, N., Fatiaki, A., Neumann, D., Carr, D., Hanlon, B., and Chahl, J., 2015, "Autonomous Chemical Vapour Detection by Micro UAV," Remote Sens., **7**(12), pp. 16865–16882.

[2] Ishida, H., Wada, Y., and Matsukura, H., 2012, "Chemical Sensing in Robotic Applications: A Review," IEEE Sens., **12**(11), pp. 3163–3173.

[3] Duan, J., Mao, S., Xie, P., Lang, J., Li, A., Tong, J., Qin, M., Xu, J., and Shen, Z., 2023, "Key Emergency Response Technologies for Abrupt Air Pollution Accidents in China," J. Environ. Sci., **123**, pp. 235–254.

[4] Dutzik, T., Scarr, A., and Casale, M., 2022, "Methane Gas Leaks: Frequent Leaks Are Resulting in Death, Injury and Other Damage to Our Health and Environment," U.S. PIRG, Environment America, Frontier Group, https://

environmentamerica.org/wp-content/uploads/2022/05/USP-MTE-FG-Methane-Gas-Leaks-Jun22-screen.pdf
[5] Hutchinson, M., Oh, H., and Chen, W.-H., 2017, "A Review of Source Term Estimation Methods for Atmospheric Dispersion Events Using Static or Mobile Sensors," Inf. Fusion, **36**, pp. 130–148.
[6] Akyildiz, I., Su, W., Sankarasubramaniam, Y., and Cayirci, E., 2002, "Wireless Sensor Networks: a Survey," Comput. Netw., **38**(4), pp. 391–552.
[7] Lu, H., Iseley, T., Behbahani, S., and Fu, L., 2020, "Leakage Detection Techniques for Oil and Gas Pipelines: State-of-the-Art," Tunnell. Underground Space Technol., **98**, p. 103249.
[8] Hoffman, K. C., Anderson, J. M., and Leang, K. K., 2024, "Rapid Airborne Gas-Plume Mapping and Source Localization With Feedforward Gas-Sensor Dynamics Compensation," ASME Lett. Dyn. Syst. Control/MECC 2024 Joint Submission, **4**(4), p. 041002.
[9] Hayes, A. T., Martinoli, A., and Goodman, R. M., 2002, "Distributed Odor Source Localization," IEEE Sens., **2**(3), pp. 260–271.
[10] Bourne, J. R., Pardyjak, E., and Leang, K. K., 2019, "Coordinated Bayesian-Based Bio-inspired Plume Source Term Estimation and Source Seeking for Mobile Robots," IEEE Trans. Rob., **35**(4), pp. 967–986.
[11] Bourne, J. R., Goodell, M., He, X., Steiner, J., and Leang, K. K., 2020, "Decentralized Multi-Agent Information-Theoretic Control for Target Estimation and Localization: Finding Chemical Leaks," Int. J. Rob. Res., **39**(13), pp. 1525–1548.
[12] Terutsuki, D., Uchida, T., Fukui, C., Sukekawa, Y., Okamoto, Y., and Kanzaki, R., 2021, "Real-Time Odor Concentration and Direction Recognition for Efficient Odor Source Localization Using a Small Bio-hybrid Drone," Sens. Actuators B., **339**, p. 129770.
[13] Peterson, J., Li, W., Cesar-Tondreau, B., Bird, J., Kochersberger, K., Czaja, W., and McLean, M., 2019, "Experiments in Unmanned Aerial Vehicle/Unmanned Ground Vehicle Radiation Search," J. Field Rob., **36**(4), pp. 818–845.
[14] Anyfantis, A., and Blionas, S., 2020, "Proof of Concept Apparatus for the Design of a Simple, Low Cost, Mobile E-Nose for Real-Time Victim Localization (Human Presence) Based on Indoor Air Quality Monitoring Sensors," Sens. Bio-Sens. Res., **27**, p. 100312.
[15] De Giudici, F., Toson, F., Piva, A., Artusi, P., Olivieri, L., and Bettanini, C., 2021, "Design and Testing of an Autonomous ARTVA Detector for Small Drones," IEEE 8th International Workshop on Metrology for Aerospace, Naples, Italy, June 23–25.
[16] Murphy, R. R., 2014, *Disaster Robotics*, MIT Press, Cambridge, MA.
[17] Yaqoob, U., and Younis, M. I., 2021, "Chemical Gas Sensors: Recent Developments, Challenges, and the Potential of Machine Learning—A Review," Sensors, **21**(8), p. 2877.
[18] Arshak, K., Moore, E., Lyons, G., Harris, J., and Clifford, S., 2004, "A Review of Gas Sensors Employed in Electronic Nose Applications," Sensor Rev., **24**(2), pp. 181–198.
[19] Monroy, J. G., Gonzalez-Jimenez, J., and Blanco, J. L., 2012, "Overcoming the Slow Recovery of MOX Gas Sensors Through a System Modeling Approach," Sensors, **12**(10), pp. 13664–13680.
[20] Gibson, D., and MacGregor, C., 2013, "A Novel Solid State Non-dispersive Infrared CO_2 Gas Sensor Compatible With Wireless and Portable Deploy," Sensors, **13**(6), pp. 7079–7103.
[21] Holzbecher, E., 2007, *Environmental Modeling: Using MATLAB*, 1st ed., Springer-Verlag, Berlin.
[22] Arulampalam, M. S., Maskell, S., Gordon, N., and Clapp, T., 2002, "A Tutorial on Particle Filters for Online Nonlinear/Non-Gaussian Bayesian Tracking," IEEE Trans. Signal Process., **50**(2), pp. 174–188.
[23] Lagzi, I., Meszaros, R., Gelybo, G., and Leelossy, A., 2013, *Atmospheric Chemistry*, Eötvös Loránd University, Budapest.
[24] Ishida, H., Nakamoto, T., and Moriizumi, T., 1998, "Remote Sensing of Gas/Odor Source Location and Concentration Distribution Using Mobile System," Sens. Actuators B, **49**(1), pp. 52–57.
[25] Li, Q., Liu, Z., and Xiao, X., 2015, "A Gas Source Localization Algorithm Based on Particle Filter in Wireless Sensor Network," Int. J. Distrib. Sensor Netw., **11**(11), p. 874532.
[26] Elfring, J., Torta, E., and van de Molengraft, M. J. G., 2021, "Particle Filters: A Hands-On Tutorial," Sensors, **21**(2), pp. 1–28.
[27] Ristic, B., Angley, D., Moran, B., and Palmer, J., 2017, "Autonomous Multi-robot Search for a Hazardous Source in a Turbulent Environment," Sensors, **17**(4), p. 918.
[28] Hutchinson, M., Oh, H., and Chen, W., 2018, "Entrotaxis as a Strategy for Autonomous Search and Source Reconstruction in Turbulent Conditions," Inf. Fusion, **42**, pp. 179–189.
[29] Bourne, J. R., and Leang, K. K., 2017, "Mutual Information Control for Target Acquisition: A Method to Localize a Gas/Chemical Plume Source Using a Mobile Sensor," ASME Dynamic Systems and Control Conference, Tysons, VA, Oct. 11–13.
[30] Hoffmann, G. M., and Tomlin, C. J., 2010, "Mobile Sensor Network Control Using Mutual Information Methods and Particle Filters," IEEE Trans. Autom. Contr., **55**(1), pp. 32–47.
[31] Cover, T. M., and Thomas, J. A., 2006, *Elements of Information Theory*, 2nd ed., John Wiley & Sons, New York.
[32] Monroy, J., Hernandez-Bennetts, V., Fan, H., Lilienthal, A., and Gonzalez-Jimenez, J., 2017, "GADEN: A 3D Gas Dispersion Simulator for Mobile Robot Olfaction in Realistic Environments," Sensors, **17**(7), p. 1479.
[33] Montgomery, D. C., 2011, *Engineering Statistics*, 5th ed., John Wiley, Hoboken, NJ.